Chapter 2

Literature Review

This chapter provides a brief overview of the literature related to the present investigation. A brief introduction to Mg and its alloys is provided at the beginning of this chapter. Then, the theories of creep, tensile, compression, and corrosion were presented. A detailed review of the current research on the creep, tensile, compression, and corrosion behavior of Mg and Mg alloy-based nanocomposites has been introduced next to the respective theory. Finally, the motivation behind the present work, as concluded from the literature review, is provided at the end of this chapter.

2.1 Designation of magnesium (Mg) alloys

The nomenclature of magnesium (Mg) alloys adheres to a standardized alpha-numeric system, wherein each alloy designation consists of alphabetical prefixes denoting major alloying constituents, followed by numerical suffixes indicating their respective weight percentages. The Al and Zn alloyed Mg alloys are designated as the AZ series. Depending on the contents of Al and Zn (wt.%), the AZ alloys are expressed as AZ91, AZ61, and AZ31, where the Al content is 9.0, 6.0, and 3.0 (wt.%), respectively, and the Zn content is 1.0 (wt.%) for each alloy. The Al and Mn alloyed Mg alloys are known as the AM series. In this series, the popular alloys are AM50 and AM60, where the Al content is 5.0 and 6.0 (wt.%), respectively, and the Mn content is less than 0.5 (wt.%) in both alloys. Thus, a zero is used for the element if its content is ≤0.5 (wt.%) in the alloy. The Mg-Al-Ca-based alloys are designated as AX series. In the present thesis, a Mg alloy consisting of 5.0Al, 2.0Ca, and 0.3Mn (wt.%) is fabricated. Therefore, according to the standard notation, the alloy is designated as AXM520. The standard alphabetic symbols used for the various alloying elements in Mg are shown in Table 2.1 [50].

2.2 Role of selected alloying elements in Mg alloys

Aluminium (Al): Al is one of the common alloying elements added to pure Mg. Al addition enhances the room temperature strength of pure Mg by solid solution strengthening. The hardness of pure Mg also increases owing to the addition of Al. The alloying of Al also improves the castability of pure Mg [50].

Table 2.1 Abbreviations used for the alloying elements added to Mg [50].

Element	Symbol	Element	Symbol	Element	Symbol
Aluminium	A	Lithium	L	Tin	T
Bismuth	B	Manganese	M	Yttrium	W
Copper	C	Nickel	N	Calcium	X
Cadmium	D	Lead	P	Antimony	Y
Rare Earths	E	Silver	Q	Zinc	Z
Iron	F	Chromium	R		
Strontium	J	Silicon	S		

Calcium (Ca): The addition of Ca significantly improves the creep and corrosion resistance of pure Mg. Adding Ca also enhances the oxidation resistance of Mg melt during casting [51,52].

Manganese (Mn): Mn improves the corrosion resistance of Mg alloys by eliminating Fe impurities present in the Mg alloys. However, the limited solid solubility of Mn in Mg limits its concentration in Mg [50].

2.3 Mg-Al-Ca alloys

The Mg-Al-Ca (AX) alloys are known for their superior creep and corrosion resistance among the Mg-Al-based alloys. The Ca/Al ratio plays a crucial role in the microstructural, mechanical, and corrosion behavior of the AX alloys. Linag et al. [53] mentioned that the formation of the β-$Mg_{17}Al_{12}$ phase was suppressed when Ca content was above 1.0 (wt.%) in the AM50 alloy. The Ca/Al ratio strongly governs the formation of the Ca-rich intermetallic phases in the AX alloys. The presence of the β-$Mg_{17}Al_{12}$ phase was reported when the Ca content was lower than 0.8 (wt.%) in the AM50 alloy. In addition to the β-$Mg_{17}Al_{12}$ phase, the Al_2Ca phase was detected in several AX-based alloys. Suzuki et al. [54] studied the solidification pathways of the AX alloys and mentioned that the formation of the Al_2Ca phase took place by a solid-state diffusion of the $(Mg,Al)_2Ca$ phase. The Ca addition influences the formation of three Ca-rich intermetallics having AB_2 stoichiometry which is known as the Laves phase. These

intermetallics are Mg_2Ca (HCP, Pearson symbol hP12, space group P63/mmc (194) and Strukturbericht notation $MgZn_2$ (C14)), $(Mg,Al)_2Ca$ (Double hexagonal crystal structure, Pearson symbol hP24, space group P63/mmc (194) and Strukturbericht notation $MgNi_2$ (C36)), and Al_2Ca (Cubic crystal structure, Pearson symbol cF24, space group $Fd\bar{3}m$ (227), and Strukturbericht notation $MgCu_2$ (C15)). The schematics of the various laves phases form in the Mg-Al-Ca alloys is shown in Figure 2.1 [55].

The C14 phase is more brittle than the C36 and C15 phases. The AX alloys undergo failure in a more brittle manner as the concentration of C14 phase increased in it [56]. The Mg-based micropillar studies of the laves phases showed that the co-deformation of the C36 phase with the α-Mg phase was noticeable rather than the C15 phase [57]. However, both these phases exhibited remarkable strengthening effects on the α-Mg phase and improved the strength of the alloy. The formation sequence of the laves phases strongly depends on the Ca content and Ca/Al ratio in the AX alloys. Zubair et al. [58] concluded that the C36 phase in the AX alloy remains stable up to 773 K. Among the laves phases form in the AX alloys, the C15 phase has the highest thermal stability owing to its higher melting point (1352 K). Therefore, the presence of the C36 and C15 phases in the AX alloys strongly influences their high-temperature properties. As the concentration of Ca decreases in AX alloys, the phases appear in the sequence of Mg_2Ca, $(Mg,Al)_2Ca$, Al_2Ca, and β-$Mg_{17}Al_{12}$. The increased concentration of Ca greatly improves the morphology of the precipitate phase, as shown in Figure 2.2 [59]. The magnified micrographs exhibit that the interlamellar spacing between the secondary phase decreases as the Al/Ca ratio increases in the AXM alloy. This also improved the strength of the alloy. However, the increased (wt.%) of Ca deteriorates the ductility of the AX alloys, which is attributed to the mechanical property mismatch between the α-Mg and laves phases [35]. The laves phases are thermally stable, resulting in superior creep resistance of the AXM alloys. In heat-treated AX alloys, the C36 phase transforms into the C15 phase by a solid-state diffusion process, which helps to improve the creep resistance of the AX alloys [54,60]. The C15 phase exhibits needle-like morphology following heat-treatment of AX-based alloys, as shown in Figure 2.3 [60]. Later studies identified them as semi-coherent precipitates of the C15 phase or G.P zones [61]. The alloying of Mn to AX alloys forms the Al_8Mn_5 phase. Mn segregates around the C15 G.P. zones and stabilizes them at high temperature. Thus, adding Mn improves the creep resistance of Mg-Al alloys [22]. However, Mn content should not exceed 0.5 (wt.%), which deteriorates the creep property of the alloy owing to increased

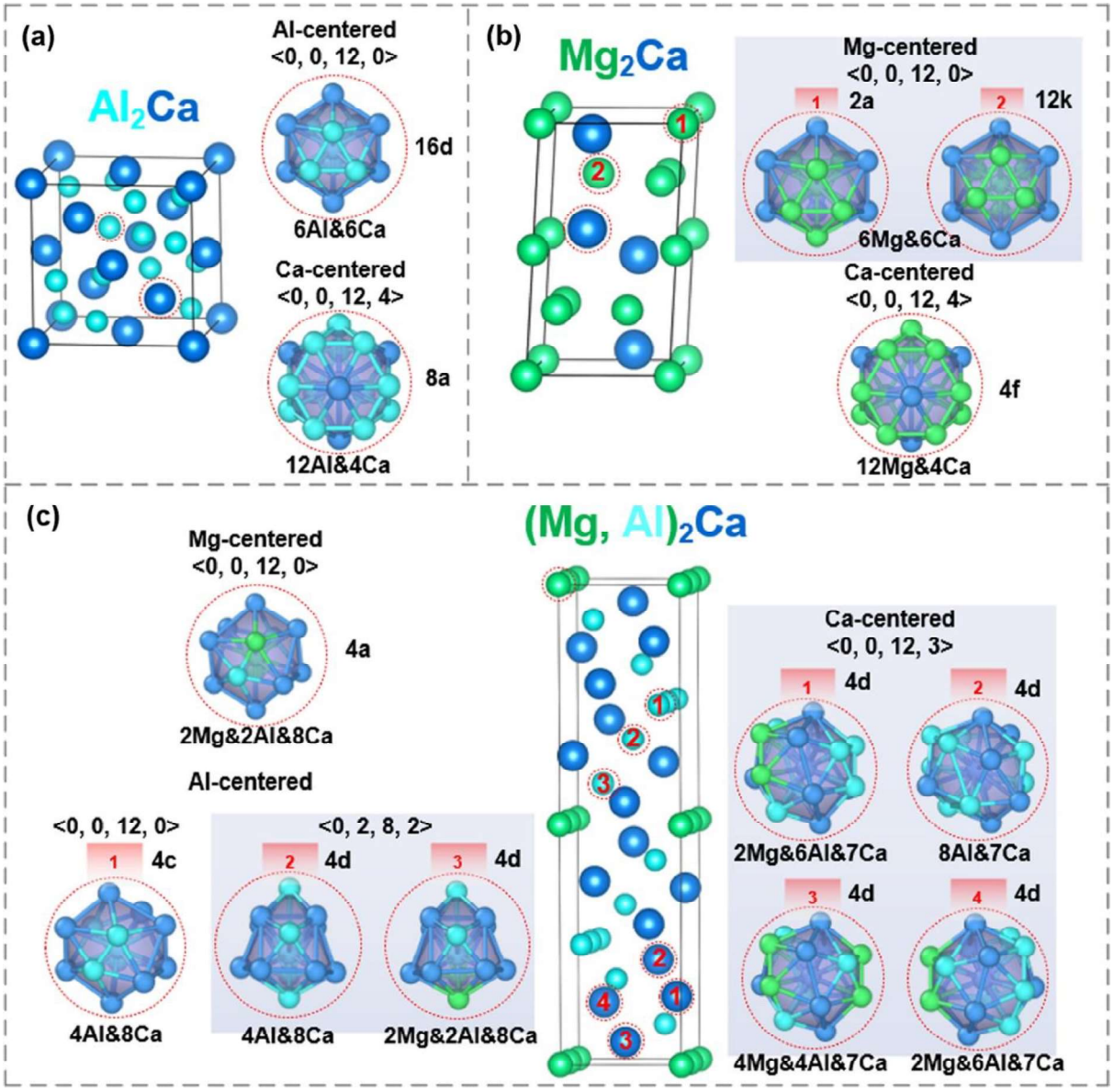

Figure 2.1 Illustration of coordination polyhedras centered by atoms at non-equivalent occupation sites in crystalline phases, including (a) C15-Al_2Ca, (b) C14-Mg_2Ca, and (c) C36-$(Mg,Al)_2Ca$. The number and type of constituent atoms in each coordination polyhedras are also shown. Wyckoff positions are shown with polyhedra. The light green, cyan, and blue spheres stand for Mg, Al, and Ca atoms, respectively [55]

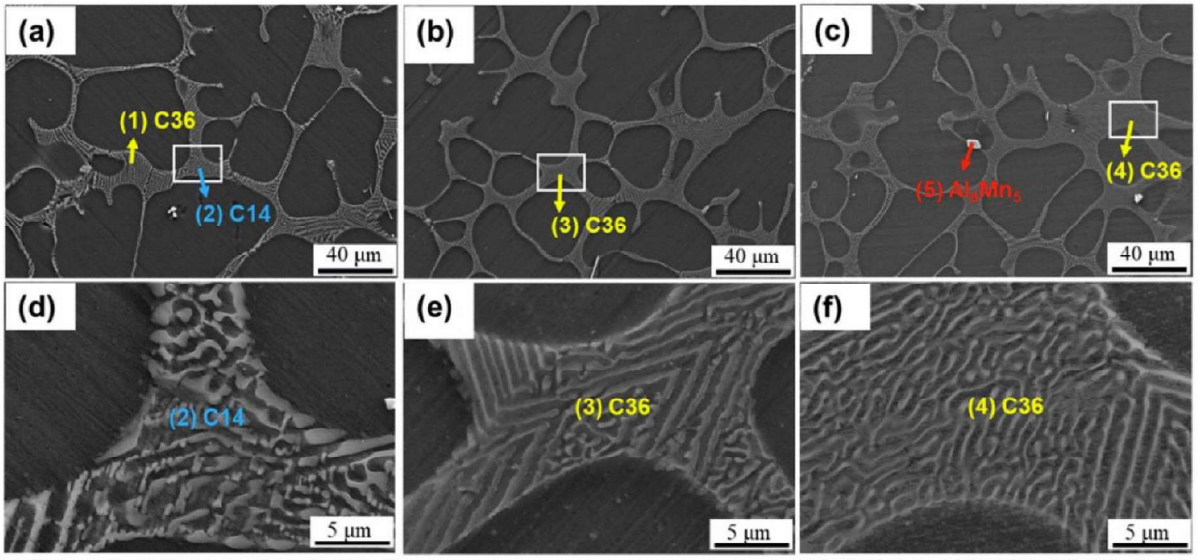

Figure 2.2 SEM micrographs of the as-cast Mg-Al-Ca-Mn alloys: (a, d) AXM530; (b, e) AXM630; (c, f) AXM730 [59].

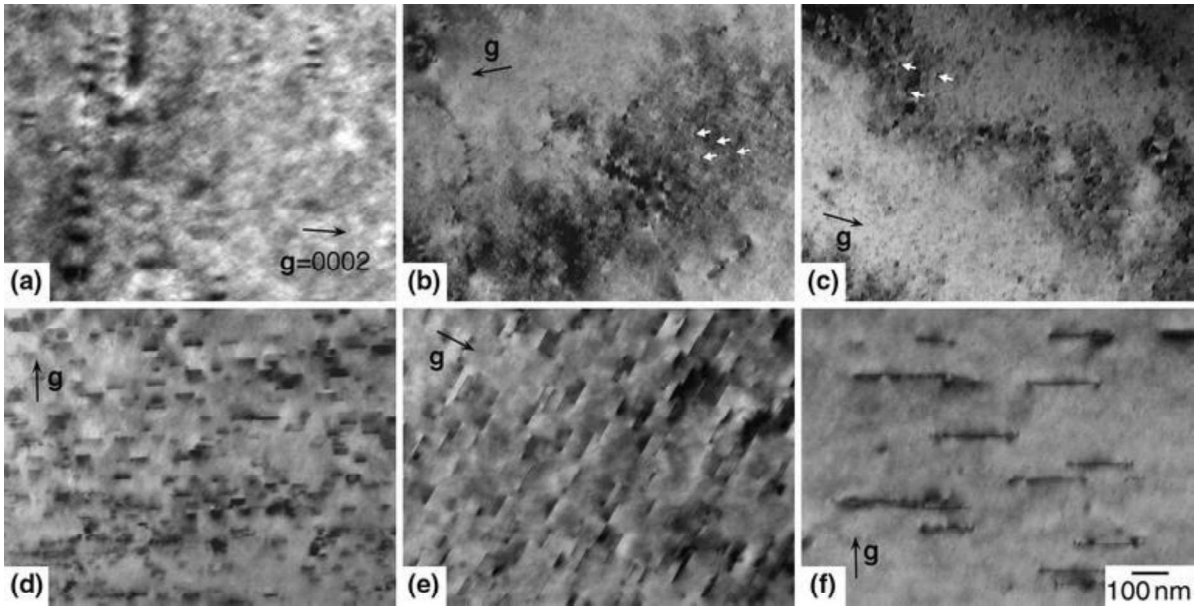

Figure 2.3 Precipitation of Al_2Ca phase in the die-cast AXJ530 alloy aged at 573 K. TEM bright-field images of the specimens aged for (a)10 s, (b) 30 s, (c) 100 s, (d) 600 s, (e) 3.6 ks and (f) 36 ks. These images were taken with B = $11\bar{2}0$ α, and **g**= 0002α. Precipitates are marked with arrows in (b) and (c) [60].

stacking fault energy. Zuo et al. [62] observed the Al_2Ca phase with Al_8Mn_5 precipitates following solutionizing and artificial aging of AXM alloy at 773 and 473 K, respectively.

2.4 Creep

Creep is a time-dependent plastic deformation of a material that is subjected to constant stress and temperature. The flow stress of a material is a function of stress and temperature. Therefore, if the test or application temperature is above absolute zero, a material undergoes deformation by the influence of both stress and temperature. However, when the test temperature is close to absolute zero, for a given stress, the deformation rate will be significantly lower because of the lower contribution from the thermal component. Thermal energy alone cannot move long segments of dislocation owing to its random nature, which can only vibrate local atoms. Thus, a small dislocation segment undergoes a climb operation using thermal energy to overcome the barrier experienced during dislocation motion. Figure 2.4(a) exhibits a schematic of the energy states of such a dislocation segment, which needs an activation energy of q to overcome the energy state 'B' while moving from 'A' to 'C' or vice-versa [63].

In order to understand the creep behavior of the material in a conventional creep test, the material is loaded uniaxially at constant stress and temperature. The strain plot of the test material as a function of time is then recorded, as shown in Figure 2.4(b). The strain rate (creep rate) plot as a function of total strain corresponding to Figure 2.4(b) is shown in Figure 2.4(c) [64]. Figure 2.4(b and c) exhibits three distinct regions of creep curve. The primary stage, or strain hardening stage, is where the strain hardening rate dominates the recovery stage, resulting in a fall in strain rate with time. In the secondary stage, the recovery rate balances the strain hardening rate, and a steady-state strain rate is attained. The steady-state creep rate has significant importance in engineering applications. The designed component should elapse the entire service period in the secondary region, allowing smooth functioning of the component.

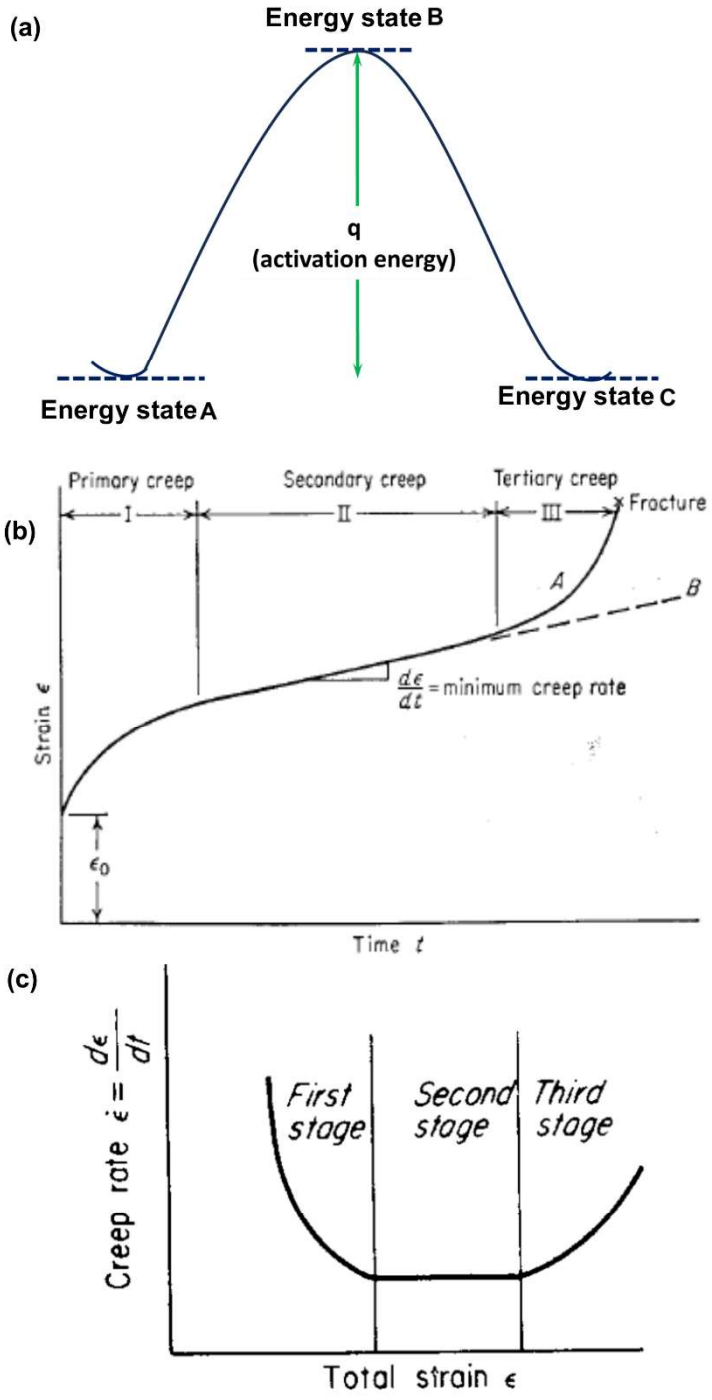

Figure 2.4 (a) Energy states of a dislocation motion while encountering an energy barrier, which interrupts its motion [63]; (b) a typical tensile creep curve showing different stages of creep; and (c) strain rate in creep test as a function of total strain [64].

2.4.1 Classification of creep mechanisms

The creep mechanism involved during the steady-state deformation of a material is predicted from the exponents of the Mukherjee-Bird-Dorn equation associated with the steady-state creep rate. The steady-state creep rate equation is expressed as follows [65]:

$$\dot{\varepsilon}_S = \frac{ADGb}{KT}\left(\frac{b}{d}\right)^p \left(\frac{\sigma}{G}\right)^n \qquad \text{Equation 2.1}$$

In Eq. 2.1 $\dot{\varepsilon}_S$ is the steady-state creep rate (s^{-1}), A is the material constant, b is the Burgers vector (Å), d is the grain size (μm), p is the inverse grain size exponent, n is the stress exponent, G is the shear modulus (MPa), k is the Boltzmann constant (= 1.38×10^{-23} m^2 kg s^{-2} K^{-1}), T is the absolute temperature (K), D is the diffusivity of the material, σ is the applied stress (MPa), and R is the universal gas constant (= 8.314 J/mol^{-1} K^{-1}).

2.4.1.1 Diffusion creep (p = 2 to 3, n = 1)

Diffusion-based creep plays a significant role when the test temperature is high, and the applied stress is significantly low $\left(< \frac{\sigma}{G} = 10^{-4}\right)$. The mechanism is governed by the diffusional flow of the vacancies and interstitials under the influence of applied stress. Depending on the vacancy flow path, the diffusion creep is further categorized as Nabarro-Herring creep (p = 2) and Coble creep (p = 3). In Nabarro-Herring creep, the diffusion flow of vacancies takes place from grain boundaries (GB) experiencing tensile stress to the GBs experiencing compressive stress (atoms flow in opposite directions) through the grain interior. Thus, the elongation of the grain took place, as shown in Figure 2.5(a). In the case of Coble creep, the vacancy diffusion occurs along the GBs, as displayed in Figure 2.5(b) [64].

2.4.1.2 Grain boundary sliding (p = 2 to 3, n = 2)

Grain boundary sliding has a limited contribution to steady-state creep deformation. However, this mechanism becomes dominant when the diffusional flow rate of the vacancies is high. To accommodate grain contiguity, GB sliding occurs during the creep deformation. In this process, GB slides relative to each other along the direction of GB, as shown in Figure 2.5(c). However, the process is not continuous and inhomogeneous, which leads to wavy GB [63].

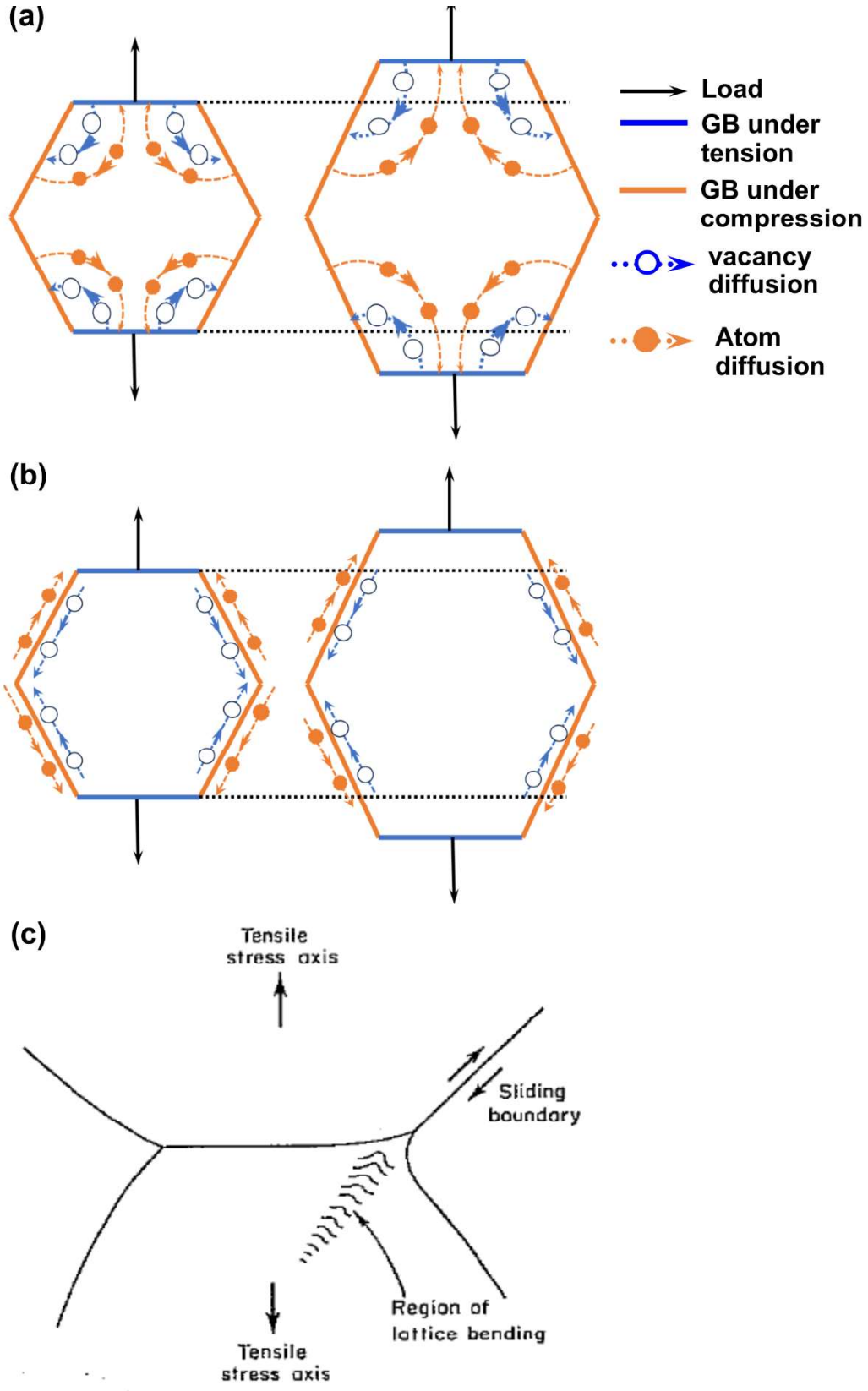

Figure 2.5 Vacancy and atom diffusion direction during (a) Nabarro-Herring, (b) Coble creep; and (c) Grain boundary sliding to accommodate the applied strain at high temperature. [63]

2.4.1.3 Dislocation creep (p = 0, n = 3 to 7)

Dislocation creep occurs by the movement of a dislocation aided by the vacancy diffusion process. The dislocation movement is achieved by glide and climb of the dislocation segment. If obstacles interrupt the dislocation glide, dislocation climbs take place to overcome the obstacle's strain field, as shown in Figure 2.6(a). Therefore, in dislocation creep, the steady-state creep rate is determined by the rate of dislocation climb. The rate of dislocation climb strongly depends on the test temperature that controls the diffusion rate of vacancies. The nature of the vacancy diffusion process can be further divided into two categories, i.e., pipe diffusion and lattice diffusion. The vacancy diffusion took place along the core of the dislocation in pipe diffusion, whereas the vacancy diffusion occurs in the entire lattice for the lattice diffusion process [64].

2.4.2 Impression creep

Impression creep is a variation of indentation creep where the indenter is a flat-bottom cylindrical punch instead of a conical-shaped indenter [66]. Thus, for an applied load, the stress is constant during the entire duration of the experiment. In this case, a flat-headed cylindrical punch is pressed against the sample surface at a constant stress and temperature. Thereafter, the penetration depth is recorded as a function of time by employing an LVDT assembly, as shown in Figure 2.6(b). The depth vs. time plot in impression creep exhibits only two stages of the creep curve, i.e., the primary and secondary stages. Unlike conventional creep, the tertiary stage is not observed in the impression creep owing to the compressive nature of the applied load. The absence of a tertiary creep stage indicates more stable deformation, making the test ideal for characterizing the creep behavior of materials. This method effectively evaluates the steady-state creep rate and creep mechanism from a small quantity test sample, making it a valuable technique for the creep behavior of materials.

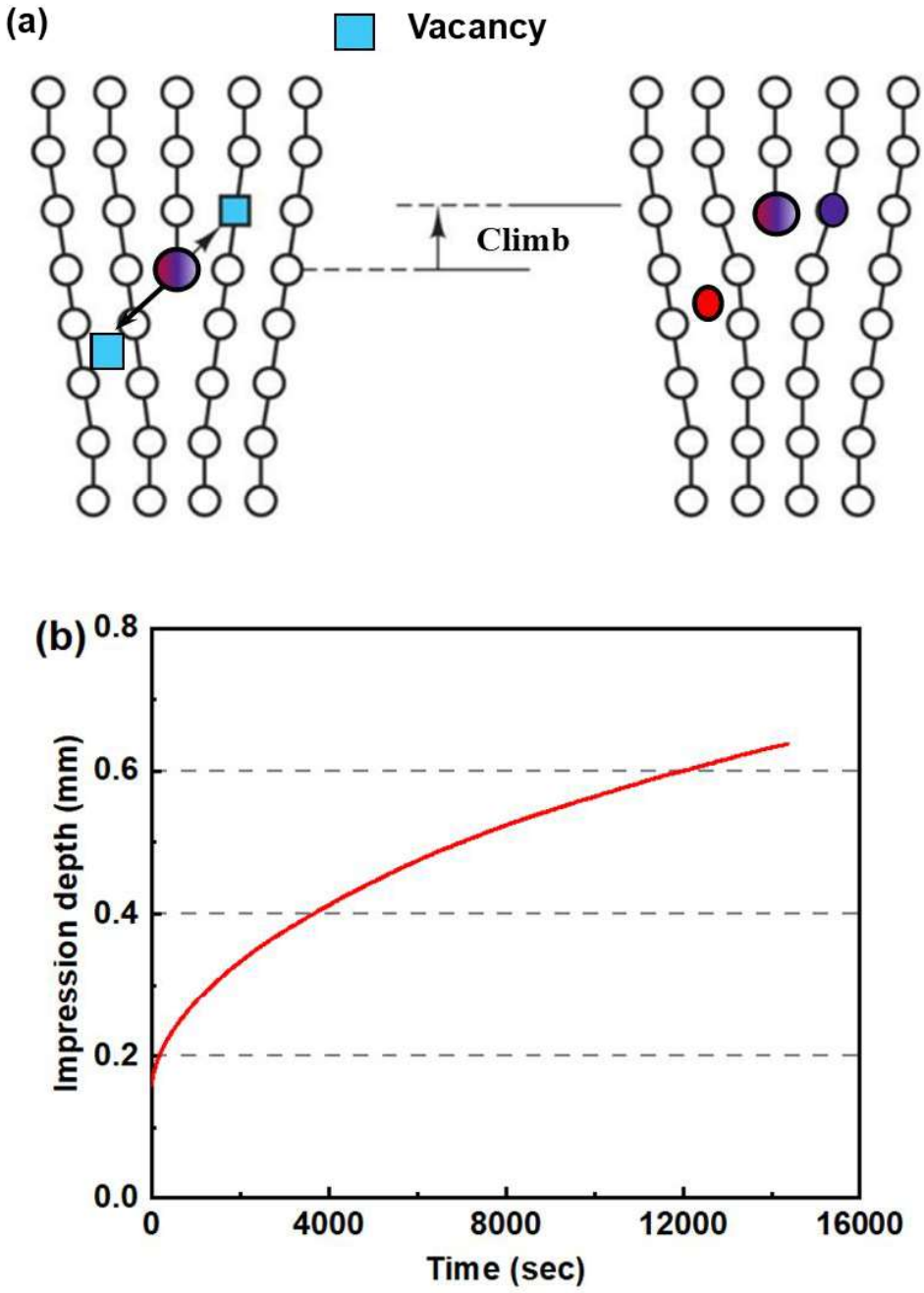

Figure 2.6 (a) A schematic exhibiting dislocation climb assisted by vacancy diffusion, and (b) a typical impression creep curve.

2.4.3 Creep behavior of pure Mg- and Mg alloy-based nanocomposites

Ferkel and Mordike [27] fabricated the Mg-SiC nanocomposite by powder metallurgy technique. They mixed 3.0 (wt.%) of 30 nm SiC powder with 40 μm Mg powder in a ball mill and then performed the hot extrusion to obtain the final nanocomposite. They reported improved creep resistance of the nanocomposite by two order compared to pure Mg. They concluded that the presence of SiC nanoparticles at the grain boundaries strongly opposed the dislocation motion and improved the creep resistance of the nanocomposites. Kastouru et al. [29] investigated the time-dependent plastic deformation of Electron21 alloy and 1.0 (wt.%) AlN reinforced Electron21. The composite was produced by stir casting. The compression creep tests of the composite were performed at 240 °C and at the stress levels of 80, 140, and 200 MPa. The AIN-reinforced Electron21 NC in their study exhibited superior creep resistance under the tested stress and temperature ranges. The calculated stress exponent (n) value of the nanocomposite was 3.3, which indicates the creep deformation mechanism was dislocation climb and glide. Kumar and Chaudhari [28] explored the creep response of the Al_2O_3-reinforced AS41 nanocomposites. The nanocomposites were made by stir casting and ultrasonic processing of the mixture of AS41 melt and 50 nm Al_2O_3 nanoparticles. The creep tests were conducted in the temperature range of 175 to 200 °C and stress range of 109.2 to 140.4 MPa. They found that the additions of 2.0 and 5.0 (wt.%) Al_2O_3 nanoparticles to AS41 improved its creep resistance. The n value was in the range of 3.0 to 6.5, indicating the governing creep mechanism was dislocation creep. The calculated activation energies for the alloy and NCs were 66.17 and 83.77 kJ/mol, indicating that the dislocation creep aided by pipe diffusion was the creep mechanism. Yang et al. [31] examined the creep response of the Electron21 alloy after reinforcing it with 0.5 and 1.0 (wt.%) AlN/Al nanoparticles. The nanoparticles were dispersed in the Electron21 melt using a high-shearing dispersion technique. The alloy and NCs were compression creep tested under the stresses of 70 and 140 MPa at 240 °C. They observed that the NCs with 0.5 (wt.%) reinforcement exhibited the lowest steady-state creep rate among the materials tested. Ganguly et al. [34] performed a creep study on the 0.6 (wt.%) Sb alloyed AZ91 alloy and its nanocomposite with 2.0 (wt.%) of 50 nm SiC nanoparticles (SiC_{np}) fabricated by the squeeze-casting process. They observed that the addition of Sb and SiC nanoparticles decreased the β-$Mg_{17}Al_{12}$ phase formation in the AZ91 alloy. They concluded that the nanocomposite's superior creep performance over the monolithic alloy was from the Orowan strengthening provided by the SiC nanoparticles. In another work, Ganguly and Mondal [30] investigated the influence of 50 nm SiC particles

additions on the creep performance of 2.0 (wt.%) Ca and 0.3 (wt.%) Sb alloyed AZ91 alloy. Microstructural and phase analysis of the alloy and NCs exhibited that the addition of SiC_{np} decreased the formation of the β-$Mg_{17}Al_{12}$ phase and increased the volume fraction of the Al_2Ca phase. The presence of the thermally stable Al_2Ca phase and SiC_{np} significantly enhanced the creep responses of the NCs. They showed that the 2.0 (wt.%) SiC nanoparticles reinforcement significantly decreased the minimum creep rate of the AZ91-2.0Ca-0.3Sb alloy under all the tested conditions. Further, they concluded that the governing creep mechanism was dislocation climb assisted by pipe diffusion. Zhou et al. [33] studied the creep behavior of Mg-9.0Al-1.0Si alloy and its nanocomposite reinforced with 60 nm SiC nanoparticles, while the test temperature and stress were varied from 448 to 498 K and 70 to 90 MPa, respectively. They observed that the addition of nanoparticles improved the creep resistance of the alloy by one order, and the creep life of the NC increased by 34.9%. They concluded that the alloy and nanocomposite deformed under the influence of dislocation creep governed by pipe diffusion. They also concluded that the nanoparticles provided additional strengthening to the alloy, which improved the creep resistance of the NCs. Ganguly et al. [67] reported the effect of 2.0 (wt.%) graphene nanoparticles (GNP) additions on the creep performance of the Mg-9.0Al-1.0Zn alloy. The alloy and GNP-reinforced composites were made using a squeeze casting setup. They observed that the addition of GNP reduced the β-$Mg_{17}Al_{12}$ phase formation, contributing to the nanocomposites' superior creep resistance. Thus, the summary of the literature review concludes that the dispersion of nanoparticles in Mg alloys significantly improved creep resistance.

2.5 Tensile and compression properties

Uniaxial tensile and compression tests are the basic tests used to measure the mechanical behavior of newly developed alloys and composites. A typical engineering stress-strain curve of a material is shown in Figure 2.7 [64]. The stress-strain plot consists of two distinct regions, i.e., elastic and plastic regions. The linear part of the curve represents the elastic region where Hooke's law is valid. The point beyond which the stress-strain curve no longer follows Hooke's law is known as the elastic limit of the material. The stress corresponding to the 0.2% offset strain is known as the yield strength (YS). The maximum stress value in the engineering stress-strain curve is known as the ultimate tensile strength (UTS) or ultimate compressive strength (UCS), depending on the loading mode. In a tensile test at UTS, the necking or localized deformation of the material starts due to an increase in stress, followed by a decrease in the

instantaneous cross-sectional area that dominates over the load-carrying capacity of the material due to strain hardening. The micro-voids and pores combine to form cracks and cause the necking of a material, leading to its failure. However, in the compression test, the micro-voids and pores close up. During compressive loading, the part of the grain rotates in the preferred direction to accommodate the given strain, which is known as deformation bands. These deformation bands further extend across the multiple grains and form shear bands that contribute to the failure of the material in compression [64].

2.5.1 Tensile and compression behavior of Mg- and Mg alloy-based nanocomposites

The effects of additions of different types of nanoparticles, i.e., Al_2O_3, ZnO, TiC, SiC, and so on, in monolithic Mg as well as Mg alloys were investigated by several researchers. Ferkel and Mordike observed that the addition of 3.0 (wt.%) SiC_{np} improved the YS and UTS of pure Mg [27]. However, the segregation of the nanoparticles at the grain boundaries resulted in the poor ductility of the Mg-SiC_{np} composites in their study. Hassan and Gupta [68] fabricated the Mg-Al_2O_3 nanocomposite (50 nm) using the disintegrated melt deposition technique. They observed an improved tensile strength with ductility of the Mg-Al_2O_3 nanocomposite produced by powder metallurgy. The Young's modulus, YS, UTS, and % El of the NCs improved by 23.1, 80.4, 42.2, and 89.2%, respectively. They concluded that the activation of non-basal slip systems in the presence of NPs improved the ductility of the NCs. They further mentioned that the grain refinement owing to the heterogeneous nucleation in the presence of NPs was beneficial. The addition of NPs changed the fracture mode of pure Mg from brittle fracture to a mixed mode of fracture. Hassan and Gupta, in another study, reported improved hardness, 0.2% YS, UTS, and ductility of pure Mg by incorporating 1.1 (vol.%) of Al_2O_3, Y_2O_3, and ZrO_2 nanoparticles [69]. They also observed that among the added NPs, the Al_2O_3 was effective in improving the tensile strength of pure Mg. The YS and UTS were improved by 46.9 and 29.5%, respectively. They concluded that the better interfacial bonding between the Al_2O_3 and Mg matrix was the reason for the enhanced tensile strength of the Mg-Al_2O_3 NCs. Interestingly, they found that the addition of ZrO_2 NPs was more effective in improving the elongation of the Mg matrix. They also investigated the effect of different sizes of Al_2O_3 particles on the mechanical properties of pure Mg [70]. The composites were manufactured by adding 50 nm, 0.3 μm, and 1μm Al_2O_3 particles in Mg melt. They observed that the addition of 50 nm particles to pure Mg improved its elongation by 89.0%. They concluded that adding nano Al_2O_3 particles

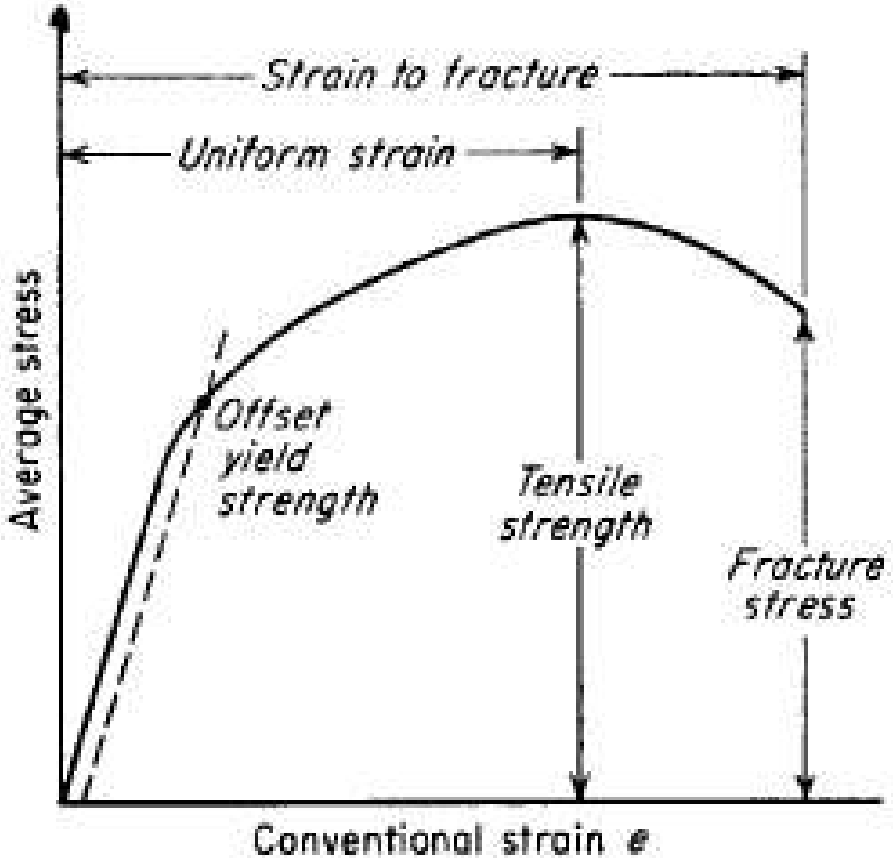

Figure 2.7 A typical engineering stress-strain curve exhibiting 0.2% yield strength, ultimate tensile strength, and fracture strength [64].

improved the ductility of pure Mg, owing to better grain refinement and distribution of the reinforcement phase. Goh et al. [71] fabricated the NCs by dispersing 0.5, 1.0, and 2.0 (vol.%) Y_2O_3 nanoparticles in pure Mg. They reported that the addition of the 2.0 (vol.%) Y_2O_3 improved the YS and UTS of pure Mg by 28.5 and 18.2%, respectively, whereas the elongation was reduced by only 1.0%. The improved strength of the NCs was attributed to the grain refinement of the NCs owing to heterogeneous nucleation during solidification. They further mentioned that the lower activity of the non-basal slip system was responsible for the low ductility of the NCs. Nguyen and Gupta [72] fabricated the AZ31B-Al_2O_3 NCs by mixing 0.66, 1.11, and 1.50 (vol.%) of 50 nm-Al_2O_3 with the AZ31B alloy. They observed the enhancement of the CYS by 32.0% and UCS by 10.0% of the AZ31B alloy due to the addition of 1.5 (vol.%) Al_2O_3 nanoparticles. Hui et al. [73] stated that the incorporation of 0.5 (wt.%) SiC_{np} in the AZ91 alloy improved the YS, UTS, and %El by 19.0, 24.0, and 83.0%, respectively. The enhancement of the mechanical property was attributed to the grain refinement of the NCs. Paramsothy et al. [74] showed that the dispersion of Al_2O_3 nanoparticles in the AZ alloy enhanced ambient temperature tensile properties as well as compressive properties of the alloy. The fractographic analysis of the alloy and NCs reveals that both materials experienced mixed fracture modes. However, the dimple-like feature was more prominent in the factograph of NCs, contributing to the enhanced ductility of the NCs compared to the alloys. Sankaranarayanan et al. [75] fabricated two separate composites of Mg-Ti and Mg-Cu by mixing 5.6 and 3.0 (wt.%) of 140 μm Ti and 50 nm Cu particles. They concluded that the addition of nanosized particles was more effective than micron-sized particles in enhancing the mechanical behavior of pure Mg. The formation of Mg-Cu intermetallic and the distribution of Cu particles along the grain boundaries of pure Mg were responsible for the improved mechanical properties of the NCs. In a different work, Sankaranarayanan et al. reported that the incorporation of 0.16, 0.48, and 0.8 (vol.%) of 90 nm ZnO particles also improved the ambient temperature tensile and compressive properties of pure Mg [76]. The additions of ZnO increased the dislocation activity at the prismatic plane, which helped to improve the mechanical properties of the alloy. Furthermore, they mentioned that the dislocations were successfully pinned by the ZnO nanoparticles, which enhanced the strength of the composites. Khosroshahi et al. [77] investigated the effect of TiO_2, SiC, and Al_2O_3 nanoparticles on the mechanical properties of AZ80 Mg alloy. Among the NCs, the SiC-reinforced AZ80 composite exhibited superior YS and ductility, owing to a better distribution of SiC nanoparticles. Meenashisundaram et al. too observed the enhancement of ambient temperature tensile and compressive properties of monolithic Mg after adding 2.0 (wt.%) TiO_2 nanoparticles [78]. The

nanocomposite containing 2.5 (wt.%) of nanoparticles exhibited enhanced YS and UTS by 37.0 and 9.0%, respectively, in their study. Katsarou et al. [29] reported the enhancement of ambient temperature CYS of the AIN-dispersed Elktron21 nanocomposite. Chen et al. [79] studied the dynamic compressive loading response of the Mg-4.0Zn-3.0Gd-1.0Ca alloy containing 2.0 (wt.%) ZnO nanoparticles. They concluded that the nanoparticles hindered the growth of twins at grain boundaries, resulting in enhanced YS of the nanocomposites. Parande et al. [80] too observed the enhanced ambient temperature tensile properties of pure Mg by the dispersion of nano-NiTi (Nitinol). Furthermore, Ganguly et al. [81] also reported the enhancement of ductility and tensile properties of the AZ91-Ca-Sb alloy by adding 0.5, 1.0, and 2.0 (wt.%) SiC_{np}. Chen et al. [82] investigated the effect of different sizes of SiC on the mechanical properties of Mg-2.0Zn-0.1Y alloy. They reported that the nanosized SiC particles greatly enhanced the strength and ductility of the alloy.

2.6 Corrosion

Corrosion is a reaction that occurs with a material and its surrounding environment, resulting in the deterioration of the material [83]. All environments are mildly or aggressively corrosive to all kinds of metals. In real life, all the mediums, for example, water, air, moisture, gas, steam, alkaline, acidic etc., tend to corrode the material. The corrosive nature of the inorganic materials is higher compared to the organic materials. Apart from this, catastrophic environments involving high temperature and pressure also significantly influence the material's corrosion behavior [83]. Therefore, in the course of selecting the structural material, it is essential to consider the corrosion behavior of the material in the targeted environment. Depending on the nature of the corrosive medium, corrosion can be classified as (a) wet corrosion and (b) dry corrosion.

The corrosion that takes place in the presence of a liquid environment is known as wet corrosion. The structural materials that undergo marine transport services are often exposed to Cl-rich water, which leads to severe corrosion of those components under wet conditions. Dry corrosion occurs in the absence of a liquid medium. In these cases, gases act as a corrosive medium. In various high-temperature reactors, the flue gases can impart dry corrosion on the structural material.

Magnesium (Mg) is known to have poor corrosion resistance among structural materials. Mg corrosion becomes significant when it contains specific elemental impurities like iron, nickel, cobalt, and copper. They act as cathodes and lead to the degradation of Mg. Mg becomes vulnerable to corrosion when exposed to species like Cl^-. The electromotive force series shows that the -2.37 V is the standard electrode potential of Mg in interaction with a solution containing Mg^{2+}. The value is the lowest among the metals used for the structural components, leading to its significant corrosion of the Mg. Therefore, Mg and Mg-based alloys are affected by several corrosion mechanisms, which are discussed in the following section [84].

2.6.1 Galvanic corrosion

Galvanic corrosion is usually identified by the severely corroded localized regions that are close to the cathode. The cathode can be a separate metal in close contact with Mg or a secondary phase in the Mg-based alloys [84]. In the internal case, the secondary intermetallic phase, like β-$Mg_{17}Al_{12}$, severely damages the α-Mg phase, causing it to defoliate from the alloy. The rate of galvanic corrosion is affected by several key factors, namely potential difference, separation distance, and contact area between cathode and anode.

2.6.2 Pitting corrosion

Pitting corrosion results from the extremely localized corrosion attack, leading to pit formation on the metals. The diameter and depth of the pits may vary significantly, indicating inhomogeneity of the reaction process. The pit formation might lead to catastrophic failure of the component in service. The pitting corrosion's undetectability makes it a more dangerous form of corrosion for structural materials. Further, the lab experiments are unable to detect this kind of corrosion [83].

2.6.3 Intergranular corrosion

Intergranular corrosion takes place along the grain boundaries of an alloy. However, the intergranular corrosion of Mg-based alloy is not significant owing to the comparably more cathodic intermetallic phase formation than the α-Mg phase. Therefore, the corrosion in Mg alloys is unable to penetrate inside the crystal through the grain boundaries [83].

2.6.4 Stress corrosion cracking

The combined effect of tensile stress and corrosion leads to the accelerated growth of the crack tip, which leads to premature failure of the component under the same stress imparted. This

type of fracture can be transgranular and intergranular in nature. According to various studies, stress corrosion cracks lead to intergranular fractures of Mg-Al-based alloys due to the interconnected secondary phase network. The formation of MgH_2 also leads to the hydrogen embrittlement of these alloys [64,83].

2.6.5 Corrosion at elevated temperature

The oxidation rate of the Mg alloy changes proportionally with the increase in temperature. The formation of the MgO layer on the surface of the Mg alloy took place. The unstable layer of MgO deteriorates quickly, compromising the alloy's integrity. It is observed that the high-temperature oxidation rate of Mg increases as the concentration of Al, Zn alloying increases in Mg. However, several studies indicate that adding Ce, Ca, and La improves the oxidation behavior of Mg alloy more than pure Mg [83].

2.6.6 Corrosion behavior of Mg- and Mg alloy-based nanocomposites

Mg alloys reinforced with microparticles exhibited more detrimental corrosion properties than the parent alloy. Tiwari et al. [85] showed that adding 25 μm SiC particles in pure Mg significantly reduced the corrosion resistance of the micro-particle reinforced composites. The addition of micro-SiC in Mg introduced additional defects in the corrosion film owing to matrix-SiC discontinuity, which resulted in the poor corrosion resistance of the composites. Turan et al. [39] reported that adding carbonaceous particles deteriorated the corrosion properties of the AZ91 alloy. The strong galvanic corrosion between carbonaceous particles and α-Mg was responsible for the poor corrosion resistance of the composites. Zhang et al. [40] too published a similar report of micro-SiC addition in the AZ91 alloy, while corrosion was tested in a 3.5 (wt.%) of NaCl solution. They mentioned that the refinement and preferential recrystallization of the β-$Mg_{17}Al_{12}$ phase around the micro-SiC particles resulted in higher galvanic corrosion of the AZ91-SiC composites. Mondal et al. [41] compared the corrosion resistance of the AE42 alloy and its hybrid composites and reported an adverse effect of the reinforcement phases on its corrosion response. They, too, mentioned that the irregular corrosion film formation on the surface of the composites was inefficient in providing adequate corrosion protection. However, recent studies suggested that adding nanoparticles might significantly protect the Mg-based alloys from corrosion [42,43]. Ganguly et al. [44] studied the impact of SiC_{np} addition on the corrosion behavior of AZ91-2.0Ca-0.3Sb alloy and reported a decreased corrosion rate of the nanocomposites compared to the squeeze-cast alloy. They

observed that the decreased volta potential between α-Mg and β-$Mg_{17}Al_{12}$ phases was responsible for the improved corrosion resistance of the NCs. However, the factors responsible for the decrease in the volta potential were not explained. Esmaeilzadeh et al. [45] explored the corrosion performance of micro and nano-sized ZnO-reinforced WE43 alloy. The improved corrosion resistance of WE43-based nanocomposites was attributed to the grain refinement and redistribution of secondary phases achieved from the ZnO nanoparticles addition. The above review concludes that the microparticles reinforcement deteriorated the corrosion resistance of the Mg alloys, whereas, the nanoparticle dispersion improved the corrosion resistance of the Mg alloys. However, the mechanism of improvement in corrosion resistance following the nanoparticle additions in the Mg alloys, as well as the effects of volume fractions of nanoparticles on corrosion behavior, is not yet fully understood.

2.7 Motivation for the thesis

The Mg-Al-based alloys are known for their high specific strength. However, their application is restricted to ambient temperature owing to their poor high-temperature properties and corrosion behavior. The RE, Sr, and Ca alloyed Mg-Al-based alloys can be used up to 473 K. Ca is a cheaper and easily available alternative to RE elements among the mentioned elements. The newly developed Mg-Al-Ca-Mn alloy has the potential to serve at 473 K. However, automotive powertrain components demand applications beyond 473 K. The dispersion of nanoparticles in pure Mg and Mg alloys imparts significant enhancement in creep properties. Considering this, the SiC_{np}-dispersed Mg-5.0Al-2.0Ca-0.3Mn (wt.%) (AXM520) alloy and nanocomposites (NCs) are developed in the present thesis. The effects of SiC_{np}-dispersion on the microstructure, tensile, compression, creep, and corrosion behavior of these NCs are studied. Further, age-hardening improves the strength of Mg alloys. Unfortunately, to the best of the authors' knowledge, the creep behavior of age-hardened and dispersion-strengthened Mg alloys has not been explored yet. Therefore, the microstructural alteration and creep charectaristics of the squeeze-cast age-hardened AXM520 alloy with SiC nanoparticles additions are also investigated.